# Cloud optical properties retrieval and associated uncertainties using multi-angular and multi-spectral measurements of the airborne radiometer OSIRIS

5  Christian Matar[1,a], Céline Cornet[1], Frédéric Parol[1], Laurent C.-Labonnote[1], Frédérique Auriol[1], and Jean-Marc Nicolas[1]

[1] Université Lille, CNRS, UMR 8518 - LOA - Laboratoire d'Optique Atmosphérique, F-59000 Lille, France

[a] now at: GRASP-SAS, Villeneuve d'Ascq, France

*Correspondence to*: Christian Matar (christian.matar@grasp-sas.com)

**Abstract.** In remote sensing applications, clouds are generally characterized by two properties: cloud optical thickness (COT) and effective radius of water/ice particles ($R_{eff}$). Most of the current operational passive remote sensing

15  algorithms use a mono-angular bi-spectral method to retrieve COT and $R_{eff}$. They are based on pre-computed lookup tables while assuming a homogeneous plane-parallel cloud layer and without considering measurement errors and the choice of ancillary data. We use the formalism of the optimal estimation method applied to near-infrared multi-angular measurements, to retrieve COT and $R_{eff}$, and the corresponding uncertainties related to the measurement errors, the ancillary data, and the cloud model assumption. The used measurements were acquired by the airborne radiometer

20  OSIRIS (Observing System Including PolaRization in the Solar Infrared Spectrum), developed by the Laboratoire d'Optique Atmosphérique. It provides multi-angular measurements at tens of meters resolution, very suitable for refining our knowledge of cloud properties and their high spatial variability. OSIRIS is based on the POLDER concept as a prototype of the future 3MI space instrument planned to be launched on the EUMETSAT-ESA MetOp-SG platform in 2023. The used approach allows the exploitation of all the angular information available for each pixel to overcome

25  the radiance angular effects. More consistent cloud properties with lower uncertainty compared to operational mono-directional retrieval methods (MODIS-like methods) are then obtained. The framework of the optimal estimation method provides also the possibility to estimate uncertainties of different sources. Three types of errors were evaluated: (1) Errors related to measurement uncertainties, which reach 10% for high values of COT and $R_{eff}$, (2) errors related to an incorrect estimation of the ancillary data that remain below 0.5%, (3) errors related to the simplified cloud physical

30  model assuming homogeneous plane-parallel cloud and the independent pixel approximation. We show that not considering the in-cloud heterogeneous vertical profiles and the 3D radiative transfer effects lead to uncertainties on COT and $R_{eff}$ exceeding 10%.

## 1 Introduction

The role and evolution of clouds in the ongoing climate change are still unclear. Their radiative feedbacks due to

35  temperature rise or the indirect effect of aerosols are insufficiently understood and they are known to contribute to the uncertainties in the Earth future climate (Boucher et al., 2013). An accurate estimation of cloud properties is therefore

very important for constraining climate and meteorological models, improving the accuracy of climate forecast, and monitoring the cloud cover evolution. The instruments onboard Earth observation satellites allow continuous monitoring of the clouds and aerosols and retrieval of their properties from a regional to a global scale.

40  The cloud properties are retrieved using the information carried by the measurements of the reflected or transmitted radiations by the clouds. Two main optical cloud properties are generally retrieved: the cloud optical thickness (COT) and the effective radius of the water/ice particles forming the cloud ($R_{eff}$). These optical properties, along with the cloud altitude, allow to characterize the clouds at a global scale and help to determine the radiative impacts of clouds along with their cooling and warming effects (Platnick et al., 2003; Twomey, 1991; Lohmann and Feichter, 2005; Rivoire et

45  al., 2020; Yang et al., 2010). Depending on the available information, various passive remote sensing methods are operationally used in the retrievals of these optical properties. For instance, the infrared split-window technique (Giraud et al., 1997; Inoue, 1985; Parol et al., 1991) uses infrared measurements and is more suitable for optically thin ice clouds (Garnier et al., 2012). The bispectral method (Nakajima and King, 1990) which uses visible and shortwave infrared wavelength, is more suitable for optically thicker clouds. It is currently used in a lot of operational algorithms

50  and in particular with the MODIS radiometer (Platnick et al., 2003). It is also possible to use a combination of multi-angular total and polarized measurements in the visible range, such as POLDER measurements (Deschamps et al., 1994), to retrieve COT and $R_{eff}$ (Bréon and Goloub, 1998; Buriez et al., 1997).

The above-mentioned methods are subject to several sources of error. Therefore, a moderate perturbation in the retrieved COT and $R_{eff}$ can, for example, cause variations of around 1 to 2 W/m$^2$ in the estimation of cloud radiative

55  forcing (Oreopoulos and Platnick, 2008). The quantification of the retrieval uncertainties of these optical properties is therefore critical. The sources of errors originating from the measurements can be quite well evaluated along the instrument calibration process and are often considered when developing a new algorithm (Sourdeval et al., 2015; Cooper et al., 2003) but the errors related to the choice of the cloud model to retrieve the parameters and the assumption made for the radiative transfer simulations should not be overlooked. Currently, computational constraints and lack of

60  information in the measurements force the operational algorithms of cloud products (MODIS, POLDER, and others) to retrieve the cloud optical properties with a simplified 1D-cloud model. In this model, clouds are considered flat between two spatially homogeneous planes in what is known as the plane-parallel and homogeneous (PPH) assumption (Cahalan et al., 1994). Another commonly used assumption is related to the infinite dimension of the PPH cloud and treats each pixel independently without considering the interactions that occur between neighboring homogeneous

65  pixels, known as the independent pixel approximation (IPA, (Cahalan et al., 1994; Marshak et al., 1995b). The effect of these two assumptions can lead to large uncertainties and biased conclusions regarding the cloud properties (Marshak et al., 2006b; Seethala and Horváth, 2010) and the aerosol-cloud relationship (Kaufman et al., 2002; Chang and Christopher, 2016).

Considering the spatial variability of the cloud macrophysical and microphysical properties, the errors induced by the

70  use of a homogeneous horizontal and vertical cloud model have been found to depend on the spatial resolution of the observed pixel, the wavelength, and the observation and illumination geometries (Kato and Marshak, 2009; Zhang and Platnick, 2011; Zinner and Mayer, 2006; Davis et al., 1997; Oreopoulos and Davies, 1998; Várnai and Marshak, 2009).

From medium to large-scale observations greater than 1 km (e.g. MODIS: $1 \times 1$ km$^2$, POLDER: $6 \times 7$ km$^2$), the PPH approximation poorly represents the cloud variability. The subpixel horizontal heterogeneity and the nonlinear nature

75  of the COT-radiance relationship create the PPH bias that leads to the underestimation of the retrieved COT (Cahalan et al., 1994; Szczap et al., 2000; Cornet et al., 2018). The PPH bias increases with pixel size due to increase inhomogeneity. Using the bi-spectral method, the COT subpixel heterogeneity induces also an overestimation bias on the retrieved R$_{eff}$ (Zhang et al., 2012), while the heterogeneity effects appear limited with polarimetric observations (Alexandrov et al., 2012; Cornet et al., 2018). On the contrary, the microphysical subpixel heterogeneity leads to an

80  underestimation of retrieved R$_{eff}$ (Marshak et al., 2006b).

At smaller scales, errors due to IPA become more dominant. At this scale, pixels can no longer be considered infinite and independent from their adjacent pixels. The radiations pass from one column to the others depending on the COT gradient. This leads to a decrease in the radiance of pixels with large optical thickness and an increase in the radiance of pixels with small optical thickness, which tends to smooth the radiative field and thus the field of retrieved COT

85  (Marshak et al., 1995a, b). As a result, it can lead to a large underestimation of the retrieved optical thickness (Cornet and Davies, 2008). Adding to these effects, for off-nadir observations, the tilted line of sight crosses different atmospheric columns with variable extinctions and optical properties which tend to additionally smooth the radiative field (Várnai and Davies, 1999; Kato and Marshak, 2009; Benner and Evans, 2001; Várnai and Marshak, 2003). In the case of fractional cloud fields not examined under nadir observations, the edges of the clouds cause an increase in

90  radiances for high viewing angles, which by its turn, increases the value of the retrieved COT (Várnai and Marshak, 2007), while overestimating the retrieved R$_{eff}$ (Platnick et al., 2003). They are often filtered out of cloud property retrievals especially under low sun angles (Takahashi et al., 2017; Zhang et al., 2019). The illumination and shadowing effects, on the contrary, lead to the roughening of the radiative field, their influence in over and under-estimating the cloud droplet size retrievals are documented in several papers (Zhang et al., 2012; Marshak et al., 2006a; Cornet et al.,

95  2005).

The assumption of a vertical homogeneous profile inside the cloud is also questionable. The vertical distribution of the cloud droplets is important to provide an accurate description of the radiative transfer in the cloud (Chang, 2002) and obtain a more accurate description of the cloud microphysics such as the water content or the droplet number concentration. For simplicity reasons, classical algorithms assume a vertically homogeneous cloud model. However,

100  several studies show a dependency of the effective radius retrievals on the SWIR band used. These differences are explained by the non-uniformity of cloud vertical profiles and by the different sensitivities of spectral channels due to the absorption difference (Platnick, 2000; Zhang et al., 2012). Indeed, the absorption by water droplets being stronger at 3.7 μm, the radiation penetrates less deeply in the cloud than at 2.2 and 1.6 μm. Channel 3.7 is therefore expected to retrieve an effective radius that corresponds to a level in the cloud higher than that of channels 2.2 and 1.6. Considerable

105  vertical variation along the cloud profiles is confirmed by many in-situ studies of droplet size profiles and water content as summarized in (Miles et al., 2000). This vertical variation in liquid particle size is an important cloud parameter related to the processes of condensation, collision-coalescence, and the appearance of precipitation (Wood, 2005).

In the operational algorithms, the retrieval of COT and R$_{eff}$ is achieved through pre-computed Look-Up Tables (LUT). This method can be used to process large databases automatically. Its disadvantage is that a modification of the particle

110  model or any other model parameter requires re-generating all these pre-calculated tables. But most importantly it lacks also the ability to assess the uncertainties on the retrieved properties.

In this paper, we present a method to overcome these drawbacks and apply it to the measurements of the airborne radiometer OSIRIS (Observing System Including PolaRization in the Solar Infrared Spectrum, (Auriol et al., 2008) which was developed in the Laboratoire d'Optique Atmosphérique (Lille, France). OSIRIS is the airborne simulator

115  of the 3MI (Multi-viewing Multi-channel Multi-polarization Imaging) radiometer, planned to be launched on MetOp-SG in 2023. It can measure the degree of linear polarization from 440 to 2200 nm and has been used onboard the French research aircraft, Falcon-20, during several airborne campaigns: CHARMEX/ADRIMED (Mallet et al., 2016), CALIOSIRIS and AEROCLO-sA (Formenti et al., 2019).

We couple the multi-angular multi-spectral measurements of OSIRIS with a statistical inversion method to obtain a

120  flexible retrieval process of COT and $R_{eff}$. The exploitation of the additional information on the cloud provided by these versatile measurements implies the use of a more sophisticated inversion method compared to the LUT. The used algorithm is based on the optimal estimation method (Rodgers, 1976, 2000) which has been widely used for applications in cloud remote sensing (Cooper et al., 2003; Poulsen et al., 2012; Sourdeval et al., 2013; Wang et al., 2016). In this method, the bayesian conditional probability together with a variational iteration method allows the

125  convergence to the physical model that best fits the measurements. Therefore, it introduces the probability distribution of solutions where the retrieved parameter being the most probable, with an ability to extract uncertainties on the retrieved parameters.

This article is organized as follows. Section 2 describes the basic characteristics of OSIRIS and some essential details of the campaign CALIOSIRIS-2. In section 3, a detailed description of the retrieval methodology is presented,

130  including the mathematical framework needed to compute the uncertainties on the retrieved cloud properties. In section 4, a case study of a liquid cloud is presented and analyzed. We assessed the magnitude of different types of errors, such as the errors due to measurement noise, the errors linked to the fixed parameters in the simulations, and the errors related to the unrealistic homogeneous cloud assumption. The multi-angular retrievals and uncertainties are compared with the results obtained by the classical mono-angular retrieval algorithms (MODIS-like method) in section 5. Finally,

135  section 6 gives a summary and some concluding remarks.

## 2 Instrumentation and airborne campaign

We use the new imaging radiometer OSIRIS. We will go through the main characteristics of the instrument and the airborne campaign CALIOSIRIS. More details about OSIRIS can be found in (Auriol et al., 2008).

### 2.1 OSIRIS

140  OSIRIS (Observing System Including PolaRisation in the Solar Infrared Spectrum, (Auriol et al., 2008)) is an extended version of the POLDER radiometer (Deschamps et al., 1994) with multi-spectral and polarization capabilities extended to the near and short-wave infrared. This airborne instrument is a prototype of the future spacecraft 3MI (Marbach et

al., 2015) planned to be launched on MetOp-SG in 2023. It consists of two optical sensors, each one with a two-dimensional array of detectors; one for the visible and near-infrared wavelengths (from 440 to 940 nm) named VIS-

145     NIR (Visible-Near Infrared) and the other one for the near and shortwave infrared wavelengths (from 940 to 2200 nm) named SWIR (Shortwave Infrared). The VIS-NIR detector contains 1392×1040 pixels with a pixel size of 6.45×6.45 µm$^2$ while the SWIR contains 320×256 pixels with a pixel size of 30×30 µm$^2$. Adding those characteristics to the wide field of view of both heads, at a typical aircraft height of 10 km, the spatial resolution at the ground is 18 m and 58 m respectively for the VIS-NIR and SWIR. This leads to a swath of about 25×19 km for the visible and 19×15 km for the

150     SWIR.

OSIRIS has eight spectral bands in the VIS-NIR and six in the SWIR. Similar to the concept of POLDER, OSIRIS contains a motorized wheel rotating the filters in front of the detectors. The step by step motor allows only one filter to intercept the incoming radiation at a particular wavelength. The polarization measurements are conducted using a second rotating wheel of polarizers. Given the sensor exposure and transfer times, the duration of a full lap is about 7

155     seconds for the VIS-NIR and 4 seconds for the SWIR. Figure 1 shows the spectral response of each channel of OSIRIS. The two channels (1240 and 2200 nm) used in this study are red-colored in the figure.
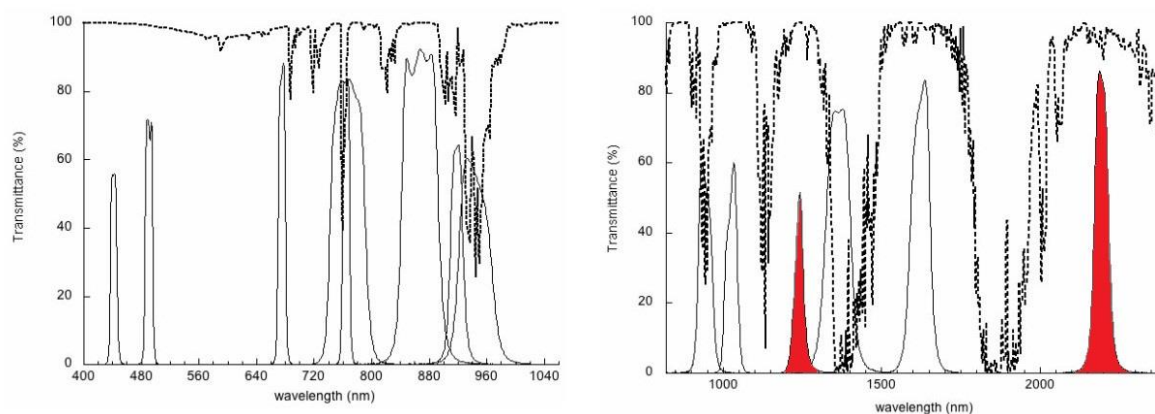
**Figure 1: Spectral wavelengths of VIS-NIR (left) and SWIR (right) optical matrices of OSIRIS. The dashed line corresponds to a typical atmospheric transmittance. The red-colored channels are used in this study (1240 and 2200 nm).**

160     OSIRIS is an imaging radiometer with a wide field of view. It has a sensor matrix that allows the acquisition of images with different viewing angles. The same scene can thus be observed several times during successive acquisitions with variable geometries. The largest dimension of the sensor matrix is oriented along-track of the aircraft to increase the number of viewing angles for the same target. For example, when the airplane is flying at 10 km altitude with a speed of 200 to 250 m/s, the same target at the ground can be seen under 20 different angles for the VIS-NIR and 19 for the

165     SWIR.

## 2.2 Airborne campaign and case study

OSIRIS participated in the airborne campaign CALIOSIRIS in October 2014. It was carried out with the contributions of the French laboratories LOA (Laboratoire d'Optique Atmosphérique) and LATMOS (Laboratoire ATmosphères,

Milieux, Observations Spatiales, Paris) and SAFIRE, the French Facility for Airborne Research. One objective of this
170    campaign was the development of new cloud and aerosol properties retrieval algorithms in anticipation of the future
space mission of 3MI intending to improve our knowledge of clouds, aerosols, and cloud-aerosol interactions.

The data used in this work focuses on a cloudy case over ocean surface. A marine monolayer cloud that was observed
on 24 October 2014 at 11:02 (local time). The aircraft flew at an altitude of 11 km above the Atlantic Ocean facing the
French west coast (46.70°,-2.82°, red arrow in Figure 2a). The solar zenith angle was equal to 59°. In Figure 2 (b), the
175    vertical profile measured by the LIDAR-LNG corresponds to the red rectangle in Figure 3b. The LIDAR-LNG detected
a monolayer cloud around 5.5 km. In the panels (c) and (d), we present colored compositions of total and polarized
radiances obtained from three spectral bands of OSIRIS over this cloud scene. The white concentric contours represent
the scattering iso-angles in a step of 10º.

The cloud strongly backscatters the total solar radiation at the three visible wavelengths, producing an intense white
180    signal. On the polarized image (Figure 2d), we observe a strong directional signature of the signal, characteristic of
scattering by spherical droplets. The main structure is the peak of polarization around 140º (known as the cloud bow),
which forms a white arc in Figure 2d. At larger scattering angles, we observe the supernumerary bows whose positions
vary with the wavelength, alternating between the red, blue, and green channels. The measured polarized signal for
scattering angles smaller than 130º is largely dominated by molecular scattering at 490 nm, hence the blue color. The
185    ocean surface modulates the scattered total and polarized radiance and increased the signal in the specular direction as
seen in the left part of Figure 2 (c) and (d).
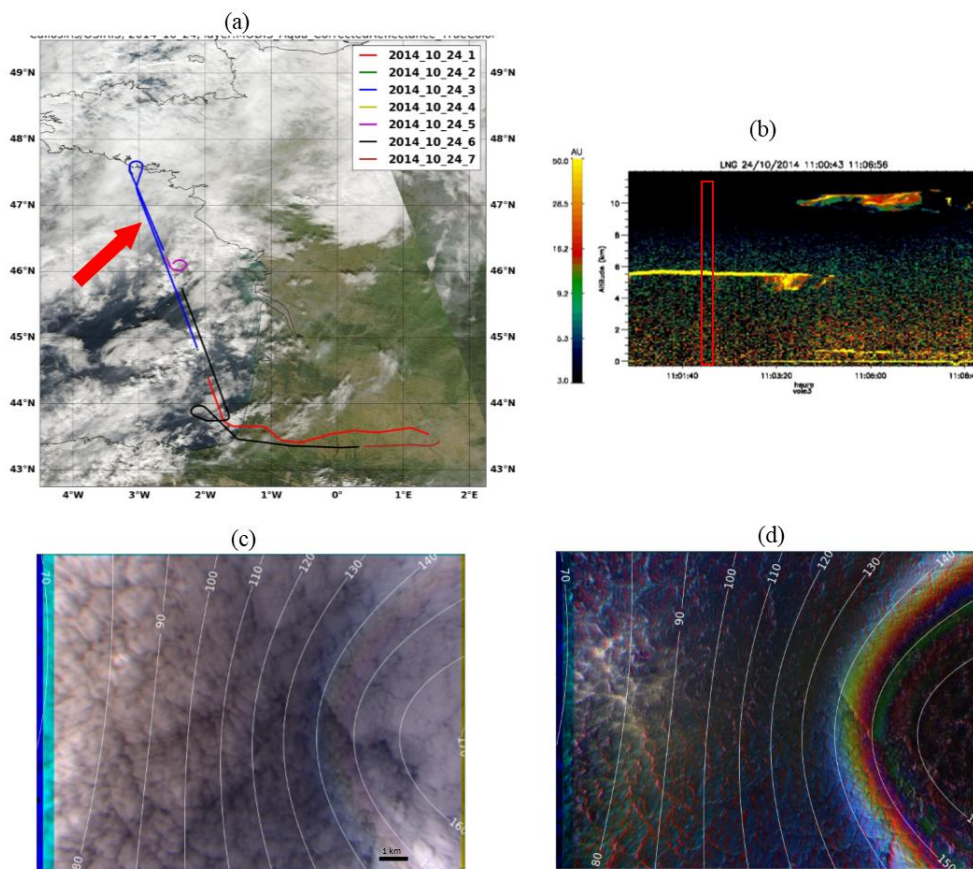
**Figure 2: Studied case on 24 October 2014 at 11:02 (local time): (a) Airplane trajectories for this day, (b) Quicklook provided by the LIDAR-LNG around the observed scene. (c) OSIRIS true-color RGB composite, obtained from the total radiances at channels 490, 670, and 865 nm. (d) OSIRIS true-color RGB composite, obtained from the polarized radiances at channels 490, 670, and 865 nm. The white concentric contours in (c) and (d) represent the scattering iso-angles in a 10º step.**

## 3 Retrieval methodology

One of the most robust approaches in cloud property retrievals is the optimal estimation method (OEM). It is increasingly used in satellite measurement inversion (Cooper et al., 2003; Poulsen et al., 2012; Sourdeval et al., 2013; Wang et al., 2016). It provides a rigorous mathematical framework to estimate one or more parameters from different measurements. The OEM also characterizes the uncertainty on the retrieved parameters while taking into account the instrument error and the underlying physical model errors. A complete description of the optimal estimation method for atmospheric applications is given by Clive D. Rodgers (Rodgers, 2000). In this book, Rodgers described exhaustively the information content extraction from measurements, the optimization of the inverse problem, and the solutions and error derivations. In the following, we will go through the basics of this method that define the core of our retrieval algorithm.

### 3.1 The formalism of the optimal estimation method

205 Considering a vector $y$ (of dimension $n_y$) containing the measurements and a state vector $x$ (of dimension $n_x$) containing the unknown properties to be retrieved, these two vectors are connected by the forward model $\mathbf{F}$, which can model the complete physics of the measurements to an adequate accuracy. The errors associated with the measurement and the modelling are represented by the error vector $\epsilon$. Eq. (1) states the relationship between these variables. Note that, hereafter, bold variables represent vectors or matrices.

$$\mathbf{y} = \mathbf{F}(\mathbf{x}) + \epsilon \qquad (1)$$

210 The OEM aims to find the best representation of parameters $x$ that minimizes the difference between simulations $\mathbf{F}(x)$ and observations $y$ while considering the linearity of the direct model near the solution. Therefore, the best estimate of the properties vector $x$ corresponds to the minimum of the so-called cost function $\mathbf{J}(x)$:

$$\mathbf{J}(\mathbf{x}) = [\mathbf{y} - \mathbf{F}(\mathbf{x})]^{\mathsf{T}}\mathbf{S}_{\epsilon}^{-1}[\mathbf{y} - \mathbf{F}(\mathbf{x})] + [\mathbf{x} - \mathbf{x_a}]^{\mathsf{T}}\mathbf{S_a}^{-1}[\mathbf{x} - \mathbf{x_a}] \qquad (2)$$

The first term of $\mathbf{J}(x)$ represents the difference between the measurements and the forward model calculated for a given state vector $x$, weighted by $\mathbf{S}_{\epsilon}$ the covariance matrix associated with the measurement error and the forward model.

215 The second term represents the difference between the state vector $x$ and the a priori state vector $x_a$ weighted by $\mathbf{S_a}$ the covariance matrix associated with $x_a$. In line with the cost function, the optimal state estimation emerges from a balance between the information carried by the measurement about the state and what we already know about it before the measurement. In our case, we do not have a prior estimate of the state vector. The iterations are initiated by a first guess while applying a large $\mathbf{S_a}$. The difference between the measurements and the forward model will be the decisive

220 element in the minimization of the cost function. It will ensure that the estimated cloud properties have the optimal fit with the observed system only.

The minimization is done through the Levenberg-Marquardt approach (Marquardt, 1963; Levenberg, 1944) based on the "Gauss-Newton" iterative method. Each iteration is calculated following the Eq. (3):

$$\boldsymbol{x}_{i+1} = \boldsymbol{x}_i + \mathbf{S}_{x_i}^{-1}\big[\mathbf{K}_i{}^{\mathsf{T}}\mathbf{S}_{\epsilon}{}^{-1}\big(\mathbf{y} - \mathbf{F}(\boldsymbol{x}_i)\big) - \mathbf{S_a}^{-1}(\boldsymbol{x}_i - \boldsymbol{x}_a)\big] \qquad (3)$$

225 where $\boldsymbol{x}_i$ is the state vector at the $i_{th}$ iteration, $\mathbf{K}_i$ is the sensitivity (or Jacobian) matrix and $\mathbf{S}_{x_i}$ is the covariance matrix of the state vector defined in Eq. (4).

$$\mathbf{S}_{\mathbf{x_i}} = \big[(1+\gamma)\mathbf{S_a}^{-1} + \mathbf{K_i^{\mathsf{T}}}\mathbf{S}_{\epsilon}^{-1}\mathbf{K_i}\big]^{-1} \qquad (4)$$

The parameter $\gamma$ affects the size of the step at each iteration. If the cost function increases at an iterative step $i$ then $\gamma$ is increased and a new smaller step $(\boldsymbol{x}_{i+1})$ is calculated until the cost function decreases.

The iterative process stops when the simulation fits the measurement (Eq. (5)) or when the iteration converges (Eq.

230 (6)). The left side of Eq. (5) represents the cost function without taking into account the a priori negligible contribution and should be smaller than $n_y$ to stop the iterations. Eq. (6) deals with the iterative steps and will make sure that the iterations will stop when the difference between two successive steps weighed by $\mathbf{S}_x$ is less than $n_x$. In other words, when further changes in the state vector have small to zero changes in the minimization.

$$[\mathbf{y} - \mathbf{F}(\mathbf{x}_i)]^{\mathrm{T}}\mathbf{S}_\epsilon^{-1}[\mathbf{y} - \mathbf{F}(\mathbf{x}_i)] \le n_y \tag{5}$$

235
$$[\mathbf{x}_i - \mathbf{x}_{i-1}]^{\mathrm{T}}\mathbf{S}_x[\mathbf{x}_i - \mathbf{x}_{i-1}] \le n_x \tag{6}$$

### 3.2 Basic setting of the retrieval algorithm

In order to apply this theoretical framework into our retrieval algorithm, we define next the basic elements stated in the previous subsection.

*The state vector* $\mathbf{x}$ contains the properties to be retrieved. In our case, they are the cloud optical thickness (COT) and

240 the effective radius of water droplets ($R_{eff}$):

$$\mathbf{x} = \begin{bmatrix} \mathrm{COT} \\ \mathrm{R_{eff}} \end{bmatrix} \tag{7}$$

*The measurement vector* $\mathbf{y}$ contains the radiances (R) measured by OSIRIS at two wavelengths and for several view directions represented in Eq. (8) (8) by $\lambda$ and $\theta$ respectively.

$$\mathbf{y} = \begin{bmatrix} \mathrm{R}_{\lambda_a}(\theta_1) \\ \mathrm{R}_{\lambda_b}(\theta_1) \\ \vdots \\ \mathrm{R}_{\lambda_a}(\theta_{n_y}) \\ \mathrm{R}_{\lambda_b}(\theta_{n_y}) \end{bmatrix} \tag{8}$$

245 *The forward model* is based on the adding-doubling approach (De Haan et al., 1987; Van de Hulst, 1963) to solve the radiative transfer equation and simulate the radiances measured by OSIRIS for the corresponding observation geometries and wavelengths. It is a major element of the retrieval and describes the radiation interaction with the cloud, the surface, and the atmosphere while fixing several parameters (e.g. wind speed, cloud altitude…). We assume a standard atmosphere with a mid-latitude summer McClatchey profile (McClatchey et al., 1972) for the computation of

250 molecular scattering. As all the channels used in the retrieval are in atmospheric windows (as seen in Figure 1), the atmospheric absorption is not accounted for. Our case study is purely above an ocean surface. The reflection by the surface can affect the measured radiances even in cloudy conditions and particularly for the optically thin clouds. The anisotropic surface reflectance of the ocean surface is characterized by a bidirectional polarization distribution function (BPDF). We used the well-known Cox and Munk model to compute the specular reflection modulated by ocean waves

255 (Cox and Munk, 1954) with a fixed ocean wind speed based on measurements of the National Oceanic and Atmospheric Administration (NOAA).

As in current operational algorithms, the cloud model used for the retrieval is a plane-parallel and homogeneous (PPH) cloud, which implies the independent column approximation (ICA). The case study is a liquid water cloud scene. Therefore, we used a log-normal distribution of liquid spherical particles (Hansen and Travis, 1974) described by an

260 effective radius and an effective variance ($v_{eff}$). The altitude of the cloud is determined by the measurements of the LIDAR-LNG that was onboard the research aircraft Falcon-20 during the airborne campaign. All simulations are monochromatic computations at the central wavelength of OSIRIS channels. The altitude of OSIRIS and the illumination and observation geometries are calculated based on the coordinates of the aircraft inertial unit.

*The Jacobian matrix* $\mathbf{K}$ includes the partial derivatives of the forward model to each element of the state vector (Eq. (9)). The columns of $\mathbf{K}$ define then the sensitivity of the radiances (each with a specific wavelength - viewing angle configuration) to COT or $R_{eff}$. The rows of the Jacobian define the sensitivity of each radiance configuration to the two retrieved properties.

$$\mathbf{K} = \begin{bmatrix} \dfrac{\partial F_{\lambda_a}(\theta_1)}{\partial COT} & \dfrac{\partial F_{\lambda_a}(\theta_1)}{\partial R_{eff}} \\ \dfrac{\partial F_{\lambda_b}(\theta_1)}{\partial COT} & \dfrac{\partial F_{\lambda_b}(\theta_1)}{\partial R_{eff}} \\ \vdots & \vdots \\ \dfrac{\partial F_{\lambda_a}(\theta_{n_y})}{\partial COT} & \dfrac{\partial F_{\lambda_a}(\theta_{n_y})}{\partial R_{eff}} \\ \dfrac{\partial F_{\lambda_b}(\theta_{n_y})}{\partial COT} & \dfrac{\partial F_{\lambda_b}(\theta_{n_y})}{\partial R_{eff}} \end{bmatrix} \tag{9}$$

### 3.3 Error characterization

During the retrieval process, every element is associated with a random or systematic error embedded in the error covariance matrix $\mathbf{S}_\epsilon$. The implantation of errors in the inverse problem adjust the solution from just a unique value of $x$ to a Gaussian probability distribution function (PDF) where $x$ is the expected value and $\mathbf{S}_x$ is its covariance.

$\mathbf{S}_x$ is calculated after a successful convergence using the Jacobian at the retrieved state and $\mathbf{S}_\epsilon$.

$$\mathbf{S}_x = \begin{bmatrix} \sigma^2_{COT} & 0 \\ 0 & \sigma^2_{r_{eff}} \end{bmatrix} \tag{10}$$

It leads to a representation of the uncertainty on a particular parameter $x_k$ defined as the square root of the corresponding diagonal element $\sigma_k = \sqrt{\mathbf{S}_{x_{kk}}}$, where $k$ is the index of the parameter in the state vector $x$ (Eq. (10)). We chose to express this uncertainty using the relative standard deviation (RSD) in % (Eq.(11)). The RSD will be used to characterize the quality of the retrieval.

$$RSD = \left(\frac{\sigma_k}{x_k}\right) \times 100 \tag{11}$$

$\mathbf{S}_\epsilon$ regroups measurement errors ($\mathbf{S}_{mes}$) and forward model errors. Indeed, the forward model $\mathbf{F}$ uses ancillary information provided by a set of fixed parameters $b$ (listed in section 3.3.2). Errors related to an uncertain estimation of these fixed parameters are represented by the covariance matrix $\mathbf{S}_{fp}$ described in the next section.

Besides the fixed parameters, the cloud model used in the radiative transfer computation adds a source of uncertainty. The uncertainties on the retrieved parameters related to these approximations are regrouped in the covariance matrix $\mathbf{S}_F$ described in the next section. $\mathbf{S}_\epsilon$ is then addressed as a sum of these three components:

$$\mathbf{S}_\epsilon = \mathbf{S}_{mes} + \mathbf{S}_{fp} + \mathbf{S}_F \tag{12}$$

Previous studies (Wang et al., 2016; Iwabuchi et al., 2016; Poulsen et al., 2012; Sourdeval et al., 2015) have already computed and presented the uncertainties on the retrieved properties for all error contributions using $\mathbf{S}_\epsilon$. The contribution of each type of error was not separated. To highlight their magnitude and better understand the sources of errors in cloud retrieval algorithms, we separate the contributions of each type of error. It is realized by propagating

the covariance matrices of errors from the measurement space into the retrieved state space (Rodgers, 2000). The gain

290 matrix $\mathbf{G_y}$ representing the sensitivity of the retrieval to the measurement is used:

$$\mathbf{G_y} = \mathbf{S_x K^T S_\epsilon^{-1}} \tag{13}$$

The total variance-covariance matrix of the retrieved state vector ($\mathbf{S_x}$) can then be decomposed into three contributions

(Eq. (14)), with each term originating from its corresponding error covariance matrix.

$$\mathbf{S_x} = \mathbf{S_{x_{mes}}} + \mathbf{S_{x_{fp}}} + \mathbf{S_{x_F}} \tag{14}$$

295 Each term in this equation is developed and discussed in the following three subsections.

### 3.3.1 Uncertainties related to the measurements

Any type of measurement is subject to errors. It is necessary to apply calibration processes to study the relationship

between the electrical signals measured by the detectors and the radiances and quantify its uncertainty. Calibration is

done during laboratory experiments before the airborne campaign or the instrument launch into space (Hickey and

300 Karoli, 1974) or in-situ if calibration sources are available onboard the sensor (Elsaesser and Kummerow, 2008). The

uncertainty of the measurements determined during calibration is usually random, uncorrelated between channels, and

can be quantified as probability density function over the measurement space.

As errors between measurements are supposed to be independent, the covariance matrix of measurement noise ($\mathbf{S_{mes}}$)

is diagonal with dimensions equal to the measurements vector dimension ($n_y \times n_y$). The diagonal elements $\sigma^2_{mes_i}$ are

305 the square of the standard deviation of measurement errors. In our retrievals, we calculated the covariance matrix based

on 5% of measurement errors that cover the measurement errors of OSIRIS: $\sigma_{mes} = R_{\lambda,\theta} \times 5\%$.

$$\mathbf{S_{mes}} = \begin{bmatrix} \sigma^2_{mes_1} & 0 & \dots & 0 \\ 0 & \sigma^2_{mes_2} & \dots & 0 \\ \vdots & \vdots & \ddots & \vdots \\ 0 & 0 & \dots & \sigma^2_{mes_{n_y}} \end{bmatrix} \tag{15}$$

The error covariance matrix for the retrieved parameters due to measurement errors is then expressed by mapping the

covariance matrix $\mathbf{S_{mes}}$ from the measurements space to the state space by using the gain matrix $\mathbf{G_y}$:

310 $$\mathbf{S_{x_{mes}}} = \mathbf{G_y S_{mes} G_y^T} \tag{16}$$

The uncertainty on a particular parameter $x_k$ originating from the measurements error is defined as the square root of

the corresponding diagonal element corresponding to the standard deviation $\sigma_{k_{mes}} = \sqrt{S_{x\,mes_{kk}}}$. It is expressed using

the *RSD (mes)* as in Eq. (11).

### 3.3.2 Uncertainties related to the fixed parameters

315 Any retrievals from remote sensing observations require prior knowledge on several unknown parameters to complete

the forward model. Those parameters are not retrieved due to a lack of sufficient information. To compute the fixed

parameters (fp) errors, we quantified the possible error in our estimation of the fixed model parameters. In our case

study, they are the altitude of the cloud (*alt*), the effective variance of the cloud droplet distribution ($v_{eff}$), and the ocean

wind speed (*ws*). These errors are set in the diagonal covariance matrix $\mathbf{S}_{\sigma fp}$. They are weighed by $\mathbf{K}_{fp}$ the Jacobian

320  matrix containing the gradient of the forward model with respect to the fixed parameters. Finally, as previously, the

errors are mapped from the measurements space to the state vector space through $\mathbf{G}_y$ to estimate their contribution in

the retrieval uncertainty as follows:

$$\mathbf{S}_{x_{fp}} = \mathbf{G}_y \, \mathbf{S}_{fp} \mathbf{G}_y^T = \mathbf{G}_y \mathbf{K}_{fp} \, \mathbf{S}_{\sigma fp} \mathbf{K}_{fp}^T \mathbf{G}_y^T \qquad (17)$$

Every column in $\mathbf{K}_{fp}$ and $\mathbf{S}_{\sigma fp}$ is dedicated to one fixed parameter. Therefore, we can separate the contributions of

325  every element of the fixed parameters vector as follows:

$$\mathbf{S}_{x_{fp}} = \mathbf{S}_{x_{fp,alt}} + \mathbf{S}_{x_{fp,ws}} + \mathbf{S}_{x_{fp,v_{eff}}} \qquad (18)$$

Each covariance matrix from the right side of Eq. (17) is developed as shown in Eq. (18). $\sigma_{b_i}$ is the standard deviation

of the fixed parameter error and $\mathbf{K}_i$ is a column vector containing the gradient of the forward model in regard of the

same fixed parameter $b_i$.

330  $$\mathbf{S}_{x_{fp,b_i}} = \mathbf{G}_y \mathbf{K}_{b_i} \sigma_{b_i}^2 \mathbf{K}_{b_i}^T \mathbf{G}_y^T \qquad (19)$$

In order to develop $\mathbf{S}_{x_{fp,b_i}}$ for each element of $\boldsymbol{b}$, the forward model has been constructed in a flexible way that permits

to initiate small variations of any fixed parameter and then calculate the partial derivatives of the forward model in

regard the ancillary data, called the Jacobians of the fixed parameters $\mathbf{K}_{alt}$, $\mathbf{K}_{v_{eff}}$, and $\mathbf{K}_{ws}$.

The last elements needed to resolve in Eq. (19) are the error standard deviations of the cloud altitude, the effective

335  variance of water droplets and the ocean wind speed, $\sigma_{alt}$, $\sigma_{v_{eff}}$ and $\sigma_{ws}$ respectively.

To estimate the uncertainties originating from the fixed cloud altitude, we used the backscattering altitudes of the

LIDAR-LNG signal obtained around the case study of CALIOSIRIS, from 11:01:06 to 11:03:06 (time where the same

cloud scene is apparent). It varies between 5.57 and 5.73 km in our cloud scene. A standard deviation of $\sigma_{alt} = 0.16$

km (3% of the cloud altitude) is then retained for the cloud altitude.

340  Concerning the effective variance $v_{eff}$, for which the polarized radiance is highly sensitive in the supernumerary arcs

near the cloud bow (Bréon and Goloub, 1998), we fixed a value of 0.02 based on the position of the cloud bows and

supernumerary arcs in the polarized radiances. After simulating radiances with several values of $v_{eff}$, we choose to add

a $\sigma_{v_{eff}} = 0.003$ (15%) possible error in the estimation of this parameter.

For the ocean wind speed fixed to 8 m/s obtained from the database of the National Oceanic and Atmospheric

345  Administration, we used an error $\sigma_{ws} = 0.8$ m/s (10%). It covers the possible sources of error in the surface wind speed

retrievals.

### 3.3.3 Uncertainties related to the forward model

Forward models are usually formulated around some limitations and assumptions that can contribute to the uncertainty

on the retrieved parameters. The forward model used to simulate the radiances measured by OSIRIS follows the cloud

350  plane parallel assumption. This assumption is known to cause errors on the retrieved parameters (see section 1) that

can be assessed and included in the total uncertainty. The evaluation of these modeling errors requires an alternative

forward model $\mathbf{F}'$ that includes more realistic physics. The contribution of this error is represented by the following equation:

$$\mathbf{S}_{x_F} = \mathbf{G}_y \mathbf{S}_F \mathbf{G}_y^T \tag{20}$$

355    $\mathbf{S}_F$ is diagonal with dimensions equals to the measurements vector dimension ($n_y \times n_y$). Each diagonal element is the square of the difference between radiance computed for a specific direction with the simplified forward model $\mathbf{F}$ and the one computed with the more realistic forward model $\mathbf{F}'$ while maintaining the same state vector and the fixed parameters vector $\boldsymbol{b}$: $\left(\mathbf{F}(\boldsymbol{x}, \boldsymbol{b}) - \mathbf{F}'(\boldsymbol{x}, \boldsymbol{b})\right)^2$.

The uncertainties related to the cloud vertical homogeneity and the cloud horizontal homogeneity are quantified
360    separately. In the following, we present the elements of the forward model used to quantify the uncertainties of these assumptions.

*Non-uniform cloud vertical profile model*

The vertically heterogeneous cloud model to assess the uncertainties of the assumed homogeneous cloud model is
365    described by:

- an effective radius profile and possibly an effective variance profile but for simplification, we will consider that $v_{\text{eff}}$ is constant over the entire vertical profile with a value of 0.02.

- an extinction coefficient ($\sigma_{\text{ext}}$) profile

- a cloud geometrical thickness (CGT) characterized by the difference between the altitude of the cloud top ($z_{\text{top}}$) and
370    the cloud base ($z_{\text{bot}}$). The values of CGT, $z_{\text{top}}$ and $z_{\text{bot}}$ are fixed based on the LIDAR measurements.

The effective radius and extinction coefficient profiles are computed using an analytical model already presented in (Merlin, 2016). It is based on adiabatic cloud profiles, which are described and used in several studies (Chang, 2002; Kokhanovsky and Rozanov, 2012). In the adiabatic scheme, the effective radius increases with altitude. However, several studies proved that a simple adiabatic profile is not sufficient to describe a realistic cloud profile (Platnick,
375    2000; Seethala and Horváth, 2010; Nakajima et al., 2010; Miller et al., 2016) because turbulent and evaporation processes can reduce the size of droplets at the top of the cloud. The description of a more realsitic vertical cloud profile is obtained with two adiabatic profiles (Figure 3) that are joined at the altitude of maximum LWC ($z_{\text{max}}$):

- The first profile from $z_{\text{bot}}$ to $z_{\text{max}}$ is considered adiabatic.

- The second profile from $z_{\text{max}}$ to $z_{\text{top}}$ follows an adiabatic LWC profile decreasing with altitude.

$R_{eff}(\mu m)$ - $\sigma_{ext}$ $(10^3 m)$
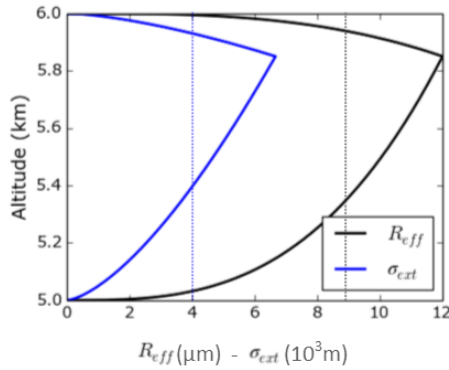
**Figure 3: The heterogeneous vertical profile of effective radius (black line) and extinction coefficient (blue line) used to assess uncertainties due to the assumption used for the vertical profile. The equivalent homogeneous vertical profiles are shown in dashed lines.**

380 Considering that LWC is equal to zero at the base and top of the cloud, and relying on the linear variation model of the LWC with altitude ($z$) established in (Platnick, 2000), we can write that:

$$\text{LWC}(z) = \text{LWC}_{\max} \frac{z - z_{bot}}{z_{max} - z_{bot}}; z \in [z_{bot}, z_{max}]$$

$$\text{LWC}(z) = \text{LWC}_{\max} \frac{z_{top} - z}{z_{top} - z_{max}}; z \in [z_{max}, z_{top}]$$

(21)

The profiles of effective radius (Eq. (22)) and extinction coefficient (Eq. (23)) can then be computed by considering that the particle concentration is constant over the entire cloud which makes it possible to obtain analytical functions of LWC, $R_{eff}$ and $\sigma_{ext}$.

$$R_{eff}(z) = R_{eff_{max}} \left( \frac{z - z_{bot}}{z_{max} - z_{bot}} \right)^{\frac{1}{3}}; z \in [z_{bot}, z_{max}]$$

$$R_{eff}(z) = R_{eff_{max}} \left( \frac{z_{top} - z}{z_{top} - z_{max}} \right)^{\frac{1}{3}}; z \in [z_{max}, z_{top}]$$

(22)

385

$$\sigma_{ext}(z) = \sigma_{ext_{max}} \left( \frac{z - z_{bot}}{z_{max} - z_{bot}} \right)^{\frac{2}{3}}; z \in [z_{bot}, z_{max}]$$

$$\sigma_{ext}(z) = \sigma_{ext_{max}} \left( \frac{z_{top} - z}{z_{top} - z_{max}} \right)^{\frac{2}{3}}; z \in [z_{max}, z_{top}]$$

(23)

A form factor $p$ (Eq. (24)) allows the adjustment of the altitude $z_{max}$ where the extinction coefficient and the effective radius are the largest:

$$p = \frac{z_{top} - z_{max}}{z_{top} - z_{bot}}$$

(24)

This unitless parameter $p$ varies from 0 to 1 representing the shape of the profile. The value 0 corresponds to $z_{max} = z_{top}$ (adiabatic cloud) and the value 1 corresponds to $z_{max} = z_{bot}$ (a reverse adiabatic cloud with a negative gradient of water content). In the following results, a value of 0.15 is assigned which allows to have a profile close to the one studied in (Miller et al., 2016) from large-eddy simulations (LES) cloud scenes.

To assess the error due to the vertical heterogeneity of the cloud, we need to specify the maximum value of the extinction coefficient $\sigma_{ext_{max}}$ and the effective radius $R_{eff_{max}}$ of the vertically heterogeneous cloud, corresponding to the "equivalent" homogeneous clouds. We use Eq. (25) to assign $\sigma_{ext_{max}}$ which leads to the same integrated exctinction profile and Eq. (26) to assign $R_{eff_{max}}$ to what ensures that the mean $R_{eff}$ of the heterogeneous vertical profile is equal to the $R_{eff}$ of the homogeneous cloud ($R_{eff_F}$). $\sigma_{ext_{max}}$ and $R_{eff_{max}}$ are found analytically by integrating the profiles described in Eq. (22) and Eq. (23).

$$\sigma_{ext_{max}} = \frac{5}{3} COT_F (z_{top} - z_{bot}) \tag{25}$$

$$R_{eff_{max}} = \frac{4}{3} R_{eff_F} \tag{26}$$

A vertically heteregenous cloud is computed for each pixel using the retrieved value based on the homogeneous assumption. The error-covariance matrix describing the error due to the simple homogenous cloud assumption (Eq. (20)) is calculated from the difference between radiances computed with homogeneous and heterogeneous vertical profiles, denoted **F** and **F'** respectively.

*The 3D radiative transfer model*

The other assumption that might affect the retrieved cloud optical properties in the current operational algorithms is the horizontally plane-parallel and homogeneous (PPH) assumption for each observed pixel. It implies that each pixel is horizontally homogeneous and independent of the neighboring pixels (known as the independent pixel approximation (IPA)). The homogeneous IPA assumption affects the cloud-top radiances and leads to differences between 1D and 3D radiances that are the result of several effects discussed in numerous publications and briefly summarized in section 1. To assess the uncertainties in the retrievals arisen from this assumption, Eq. (20) is used. $\mathbf{S}_F$ is then the difference between the radiances computed with a 1D radiative transfer code (1D-RT), following the Adding-doubling scheme (Hansen and Travis, 1974), and the radiances computed with a 3D radiative transfer (3D-RT) code called 3DMCPOL (Cornet et al., 2010). The 3D simulations used for each pixel, the COT and Reff retrieved using the PPH assumption. Errors on cloud model assumptions are assessed independently so vertical homogeneous profiles are assumed. We also assume a flat cloud top, differences, and errors are thus minimized as cloud top variation may increase the differences between 3D and 1D radiances (Várnai and Davies, 1999; Várnai, 2000).

## 420  4 Retrieval and uncertainty estimation for a liquid cloud case study measured by OSIRIS

Our strategy to assess the different types of uncertainty follows two steps. In a first step, we retrieve COT and $R_{eff}$ using a bispectral multi-angular method by considering the uncertainties related to the measurement errors alone. We use a weak absorbing channel centered at 1240 nm that is mainly sensitive to COT, and a channel partially absorbed by the water droplets centered at 2200 nm, and thus sensitive on $R_{eff}$. In this case study, up to 13 viewing angles are

425  available for each pixel. In the first step, only the measurement errors are accounted for and included in $S_\epsilon$. This error is straightforward and usually well characterized but does not change once the measurements are realized. Not considering the other errors at this stage allows benefiting from a faster retrieval algorithm without the calculation of $K_b$ and the heavy computation cost of heterogeneous cloud profiles and 3D-RT calculations. The second step consists of computing the error due to ertically and horizontally inhomogeneous cloud from the retrieved $R_{eff}$ and COT.

430  In Figure 4, COT (a) and $R_{eff}$ (b) retrieved from multi-angular SWIR radiances are presented. Spatial variations are mainly due to variations in the observed cloud structures. The COT range is between 0.5 and 6 with a mean value of 2.1 while $R_{eff}$ varies between 2 and 24 µm around a mean value of 8.8 µm.
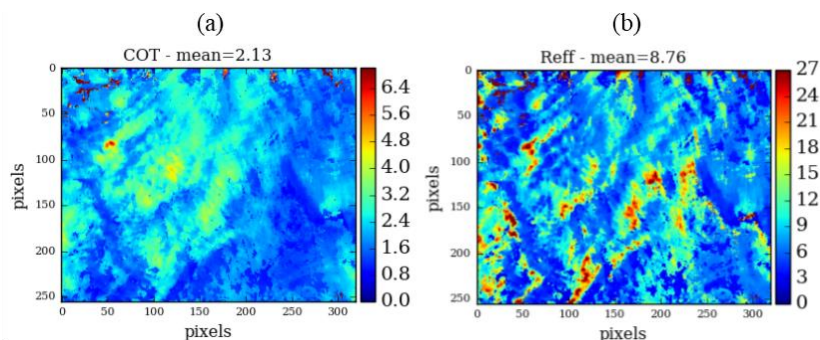
**Figure 4: COT (a) and $R_{eff}$ (b) retrieved from a liquid cloud case observed during the CALIOSIRIS airborne campaign on 30 June 2014 at 11:02 (local time).**

As detailed in section 3.3, the final error is divided into three categories. Figure 5 shows the uncertainties originating from a 5% measurement error on the retrieved COT (*RSD COT (mes)*) and $R_{eff}$ (*RSD $R_{eff}$ (mes)*). *RSD COT (mes)*

435  ranged from 0.5 to 5% with a mean value of 3.2% while *RSD $R_{eff}$ (mes)* ranged from 2 to 12% with a mean value equal to 6.2%. Both cloud properties have relative uncertainties that increase mainly with the magnitude of the retrieved values. This is related to the quasi-linearity of the radiance as a function of COT and $R_{eff}$ in this cloud regime (small COT). When the radiance-COT (or $R_{eff}$) relationship is quasi-linear, the sensitivity of the forward model to COT (or $R_{eff}$) is high, which will consequently lead to parameters retrieved with high accuracy (low RSD). As COT (or $R_{eff}$)

440  increases, the gradient of the radiance-COT (or $R_{eff}$) relationship decreases causing larger uncertainties.
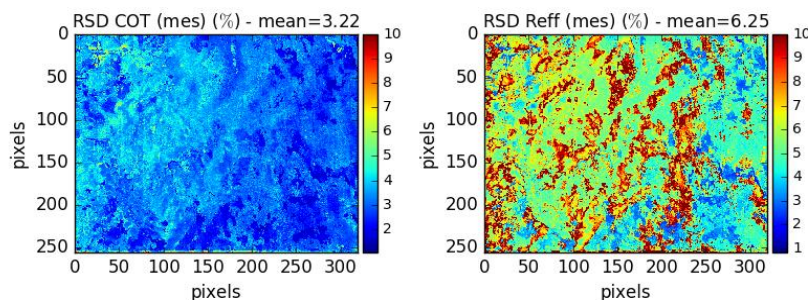
**Figure 5: Uncertainties (RSD (%)) on COT (a) and $R_{eff}$ (b) originating from the measurement errors for the case study of CALIOSIRIS.**

The second type of uncertainty is related to the fixed parameters in the forward model. In Figure 6, we show the uncertainty on COT and $R_{eff}$ in % due to an incorrect estimation of each fixed parameter in the forward model. Panels (a) and (b) represent the uncertainties originating from the fixed cloud altitude, *RSD COT (alt)* and *RSD $R_{eff}$ (alt)* respectively. Both show null values of uncertainties. In fact, in the visible range, the altitude of the cloud mainly

445  determined the amount of Rayleigh scattering that occurs above the cloud. This type of scattering is dominant at shorter wavelengths and becomes negligible at the studied wavelengths (1240 and 2200 nm). Consequently, at these wavelengths, an error in the fixed cloud altitude does not contribute to the uncertainty on the retrieved COT and $R_{eff}$.

The (c) and (d) panels in Figure 6 represent the uncertainties on the retrieved COT and $R_{eff}$ originating from the fixed effective variance of droplets. They are nearly null on COT with a mean value of 0.05% as the 15% uncertainty on the

450  value of $v_{eff}$ (0.02) does not modify the total radiances. On the other hand, *RSD $R_{eff}$ ($v_{eff}$)* reaches 0.5% with a mean value of 0.25%. Indeed, $v_{eff}$ modifies the width of the cloud droplet distribution and consequently slightly the absorption by cloud droplets, which gives information to retrieve $R_{eff}$. For $R_{eff}$ higher than 15 µm, the relationship between SWIR radiances and $R_{eff}$ tends to flatten which make them less sensitive to $v_{eff}$ and thus the uncertainties are smaller than 0.1%.

455  The panels (e) and (f) in Figure 6 shows that an error in the estimation of the ocean wind speed affects the retrieved COT and $R_{eff}$ mainly for small COT. The water-air interface is reflecting mainly in the direction of specular reflection, but the ocean is not perfectly smooth; the surface is modulated by waves that enlarge the directions of reflection due to the specular reflection. These waves are mainly formed by the wind. The higher the surface wind speed is, the greater the amplitude of the waves leading to a larger reflection angle (wider sun-glint). The Sun-glint reflection is seen by

460  OSIRIS only for very small values of COT and implies uncertainties on the retrieved parameters of about 0.5%. At higher COT, the surface is non-apparent to OSIRIS measurements, and uncertainties are thus close to zero.

We note that all the uncertainties of the studied fixed parameters remain below 1%, which shows that retrieval of all the COT-$R_{eff}$ couples does not have a high dependence on the fixed parameters.
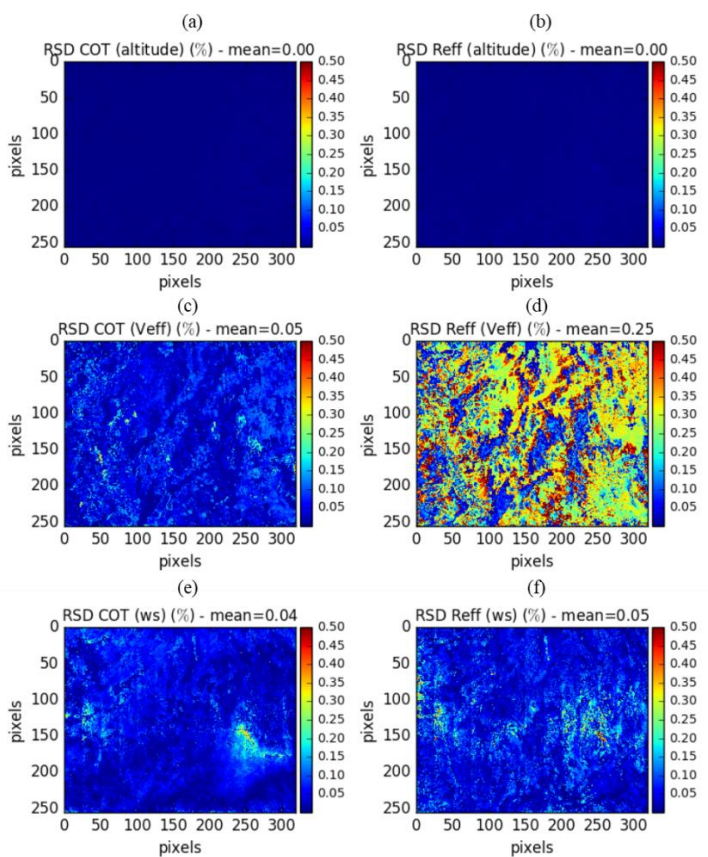
**Figure 6: The uncertainties (RSD (%)) on COT (left column) and R_eff (right column) originating from the ancillary parameter errors: altitude (a and b), the effective variance of water droplet distribution (c and d), and the surface wind speed (e and f).**

465    The uncertainties due to the assumptions of the forward model are presented in Figure 7. The panels (a) and (b) represent the uncertainties on COT and $R_{eff}$ respectively, originating from the vertically homogeneous assumption. *RSD COT (Fpv)* ranges between 1 and 8% with a mean value of 4.9% while *RSD $R_{eff}$ (Fpv)* varies from 2 to 20% with a mean value of 13.3%. We note that when the cloud is optically thin, *RSD COT (Fpv)* and *RSD $R_{eff}$ (Fpv)* tend to be lower. When the extinction is small, the radiations penetrate deeper into the cloud and bring information on the whole

470    cloud, similar to the one obtained with the homogenous vertical profile. The differences between radiances issued from the vertical heterogeneous and homogeneous profiles are small since the integrated extinction over the cloud is approximately the same in both cases. For larger COT, the radiations penetrate less in the cloud and are only affected by the upper part of the cloud where the extinction coefficient is different from one profile to another. In this case, *RSD COT (Fpv)* and *RSD $R_{eff}$ (Fpv)* are larger up to 20%.
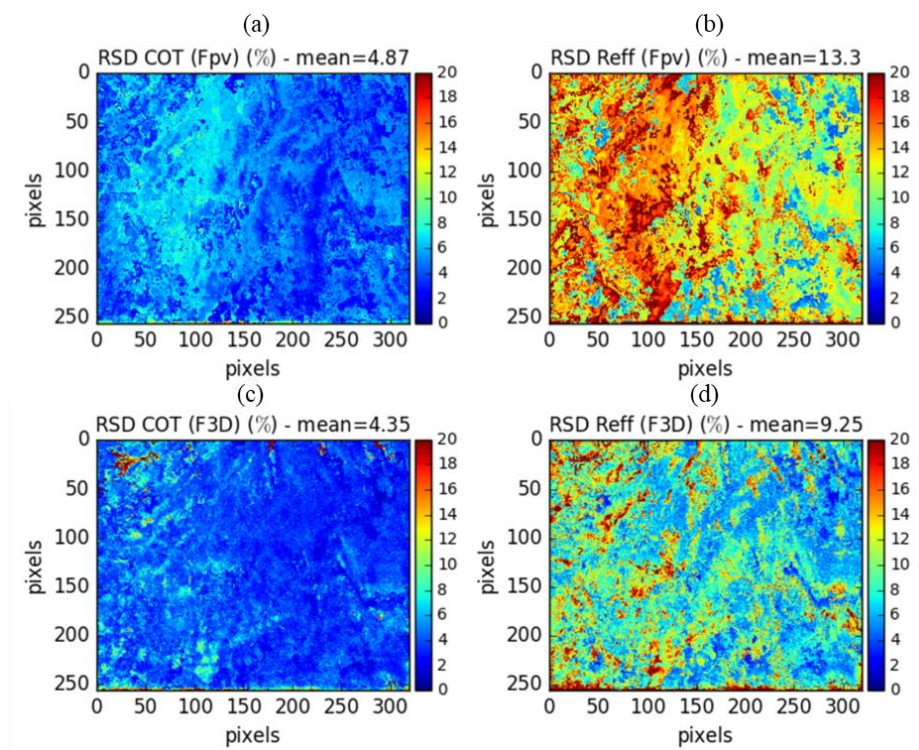
**Figure 7: The uncertainties (%) on COT and R$_{eff}$ originating from the assumptions in the forward, for not considering: the heterogeneous vertical profile (a and b) and the 3D radiative behavior of radiations (c and d).**

The uncertainties originating from the use of a 1D radiative transfer code instead of a more realistic 3D radiative transfer are represented in Figure 7 (c) and (d) for COT and R$_{eff}$ respectively. *RSD COT (F3D)* ranges between 1 and 20% with a mean value of 4.35%, while *RSD R$_{eff}$ (F3D)* varies from 2 to 18% with a mean value of 9.25%. At high spatial resolution, these differences can be caused by several effects that can add or oppose each other. Considering the solar zenith incidence angle (59º), illumination and shadowing effects can be present depending on the viewing geometries and roughness of the radiative fields (Várnai, 2000).

However, in this work, we are dealing with multi-angular measurements where the same cloudy pixel is viewed under different viewing angles, which tends to mitigate the influence of illumination and shadowing effects. Therefore, contrary to MODIS mono-angular retrieval (Várnai and Marshak, 2002), 3D effects due to solar illumination do not appear in the retrieved cloud properties.

The plane-parallel and homogenous (PPH) approximation (Cahalan et al., 1994) strongly depends on the sensor spatial resolution (Oreopoulos and Davies, 1998). The high spatial resolution of OSIRIS (around 50 m) makes the sub-pixel cloud variabilities can be fairly well represented leading to a low PPH bias. At this scale, the effects related to the Independent Pixel Approximation (IPA) are dominant since the horizontal transfers of photons between pixels are important.. The smaller these columns are considered in the simulations, the more the real behavior of radiation in the atmosphere will be misrepresented. The horizontal radiation transport (HRT) tends to smooth the radiative field as it

is shown in Figure 8. The panels (b) and (d) representing the radiances computed with 3DMCPOL at 1240 and 2200 nm respectively show the smoothest field compared to the radiances computed in 1D in (a) and (c). The variabilities in the 3D radiative field are indeed less pronounced compared to the 1D field.
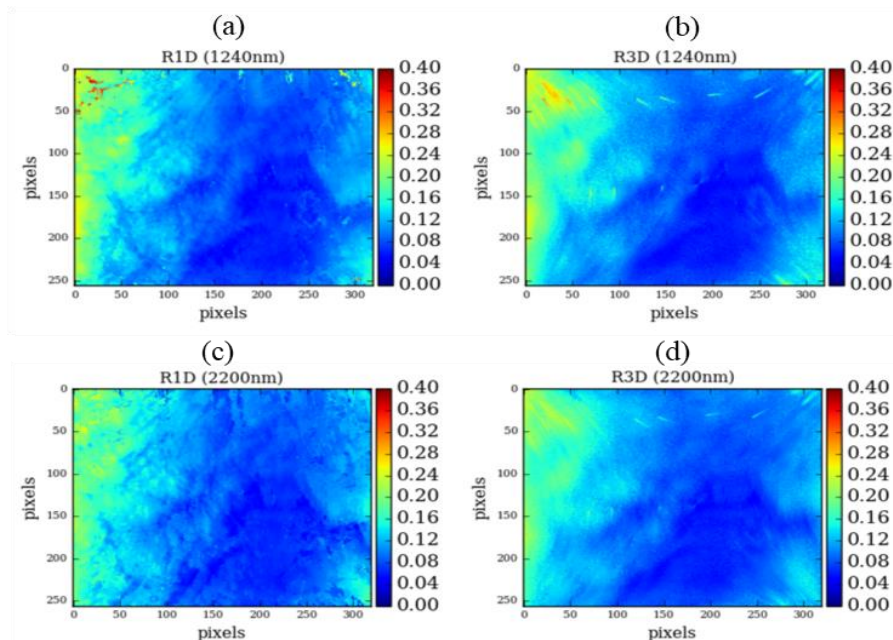
**Figure 8: The simulated 1D (a) and 3D (b) radiances at 1240 nm using the retrieved COT and R$_{eff}$ presented in Figure 4 for the central image. (c) and (d) are the same as (a) and (b) but for 2200 nm.**

495    In Figure 9, the histograms of the relative difference between the radiances computed in 1D (R1D) and the radiances computed in 3D (R3D) at 1240 nm for different bins of optical thickness are plotted. We can see the shift of the histograms from negative value for small optical thickness (R1D < R3D) towards positive difference for larger optical thickness (R1D > R3D) that is explained by the horizontal radiation transport between columns.
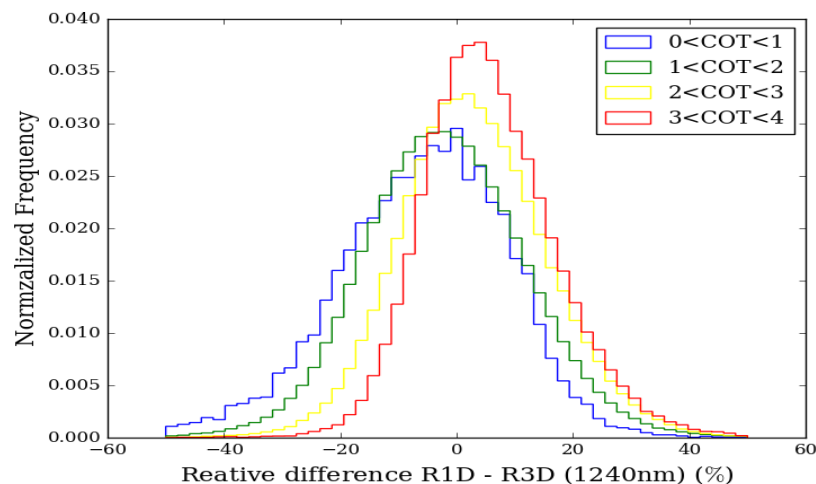
**Figure 9: Histograms of the relative difference between the radiances computed in 1D and 3D at 1240 nm for the central image. Each histogram corresponds to a domain of COT.**

500

Overall, we note that the uncertainties due to the forward model assumption are much more important than the one due to the fixed parameters. The forward model is not sensitive to small variations in the fixed parameters. However, while assessing uncertainties due to the vertical profile or radiative transfer assumptio, we change the parameters that our forward model is proven to depend on, thus minor changes in the integrated profile can lead to relatively large variations

505 in the radiance fields, and consequently large uncertainties.

## 5 Advantage of using multi-angular versus mono angular information

The same strategy applied in section 4 is applied using a bispectral mono-angular method used for the MODIS instrument for example. Using the MODIS-like approach, the measurement vector $y$ for each pixel contains two mono-angular total radiances, one at 1240 nm and the other at 2200 nm to retrieve COT and $R_{eff}$.

510
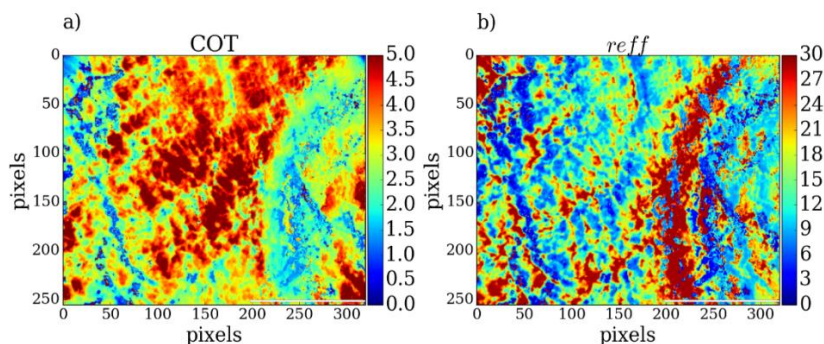
**Figure 10: COT (a) and $R_{eff}$ (b) retrieved using MODIS-like method for the CALIOSIRIS liquid cloud case study on 30 June 2014 at 11:02 (local time).**

515    The retrieved COT over the whole field varies between 1 and 12 with a mean value equals to 3.44. The range of

retrieved $R_{eff}$ has a mean value of 15.65 µm affected by the high value of $R_{eff}$ retrieved around the scattering angles

130-140° where the sensitivity of 2200 nm radiances to the water droplet size is known to be small. As a matter of fact,

(Cho et al., 2015) show indeed that in liquid marine cloud cases, the phase functions of different $R_{eff}$ converge to the

same value for these scattering angle range leading to the failure of water droplets size retrieval from MODIS

520    measurements. This reduced sensitivity explains also the high uncertainty on $R_{eff}$ due to measurement errors around

the cloud bow (Figure 11). The reduced sensitivity on $R_{eff,}$ in this case, is not limited to the cloud bow directions and

supernumerary bows but is also visible at small scattering angles (70-80°) that can be affected by specular reflection

over the ocean.
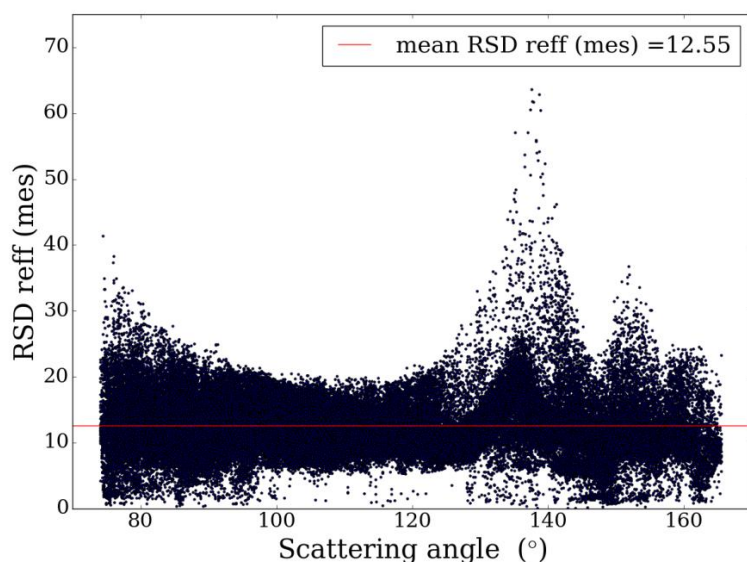
525

**Figure 11: Uncertainty on the effective radius originating from the measurement error, *RSD $R_{eff}$ (mes)* as a function of the
scattering. The red line represents the mean *RSD $R_{eff}$ (mes)* = 12.55%.**

Multi-angular retrieval presents the major advantage, that no aberrant values of $R_{eff}$ are retrieved near the scattering

angles at 140° (comparing Figure 4b to Figure 10b). Clearly, the multi-angular measurements contain more information

530    and allow to resolve the problem encountered with the MODIS-like method which is also clear in the reduction of

failed convergences from 5.9% to 2.4% (not shown here). In the overall scene, smaller $R_{eff}$ values (and consequently

lower COT values) are obtained.

The relation between radiances and COT/$R_{eff}$ being monotonical, the mono-directional method always allows us to

find a retrieved value as it is always possible to find a cloud model (a pair of COT and $R_{eff}$) that matches a single

535    measured radiance of a given target. However, this value can be more or less far from the real value and is not

necessarily an indication of an accurate retrieval, but only that a fit occurred. On the other hand, multi-angular retrieval

makes the constraining of the forward model much more challenging. It uses jointly all the available measurements.

The retrieved state is then consistent at the best with all the measurements associated with different viewing angles.

On this basis, it is not suitable to compare the cost function of a mono-directional method where one value of COT fits
540  one radiance and the cost function of a multi-angular method where one value of COT corresponds to ~13 radiances.
To overcome this problem, we compare the accuracy of the retrievals by the response of the state vector to the errors,
represented by the relative standard deviation (RSD). In Figure 12, we present the spatially average of the different
types of errors, presented in section 4, for the mono-angular method (light green for COT and light blue for $R_{eff}$) in
comparison with the multi-angular method (dark green for COT and dark blue for $R_{eff}$). We divide the source of errors
545  in two panels, the left panel groups the lowest values of RSD and the right panel for the highest values of RSD.

Overall, $R_{eff}$ uncertainties are larger than the one on COT for any type of error. In the left panel of Figure 12, the three
fixed model parameters errors related to an incorrect estimation of the fixed parameters of the model are weak
compared to the others and remain below 0.3% for mono-angular retrievals. As explained in section 4, the fixed altitude
does not contribute to the uncertainty on the two retrieved parameters. The average uncertainties originating from the
550  fixed value of $v_{eff}$ are about 0.05% for COT and slightly higher (0.15%) for $R_{eff}$ since $v_{eff}$ affects the cloud bows that
are also sensitive to $R_{eff}$. Concerning the surface wind speed, the uncertainties are around an average of 0.05%.

In the right panel, for mono-angular retrieval, the measurement error contributes to the uncertainty of about 8% on the
retrieved COT and of about 12% on the retrieved $R_{eff}$. The uncertainties are reduced by a factor two with multi-angular
retrieval. The multi-angular approach leads indeed to more information available for each cloudy pixel and each
555  additional information reduces the uncertainty on the retrieved parameters in the presence of the same 5% random
noise in the measurements.

The following two groups of bars correspond to the to the error introduced by the homogeneous assumption in the
forward model. They are the main source of errors. For mono-angular retrieval, the assumption of a vertical
homogenous profile contributes to an uncertainty of about 16% on COT and 54% on $R_{eff}$. These uncertainties are
560  reduced by a factor four in the case of multi-angular retrieval. As discussed previously, the principal effects of 1D
assumptions errors at the spatial resolution of OSIRIS come from the non-independence of the cloud columns that lead
to smooth the 3D radiative fields. They lead to an uncertainty of 28% on COT and 45% on $R_{eff}$ when a mono-angular
instrument is used.
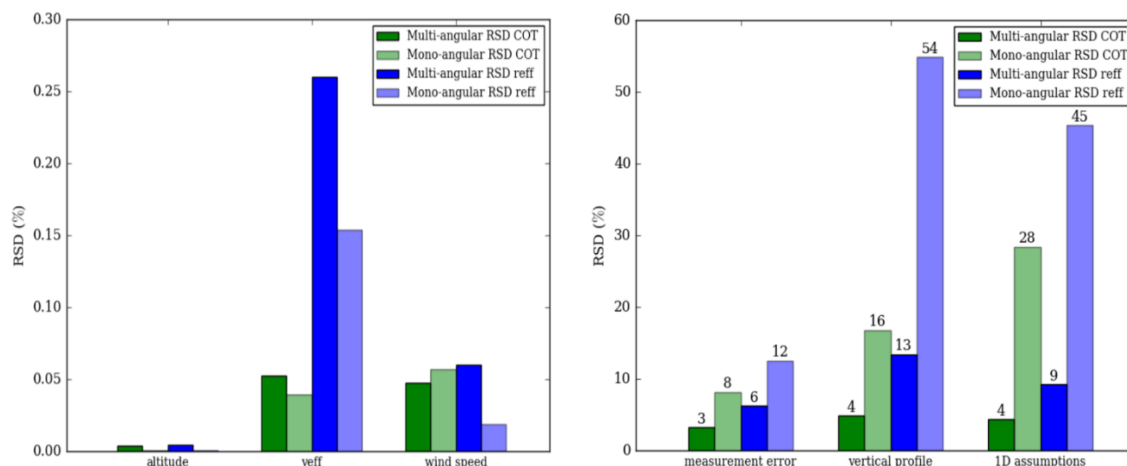
**Figure 12: Bar chart of the mean uncertainties on the retrieved COT and $R_{eff}$: green bars correspond to RSD COT and blue bars to RSD $R_{eff}$. Dark colors correspond to multi-angular retrieval and light colors to mono-angular retrieval. The errors originating from the fixed parameter errors are in the left panel and the measurements and forward model errors in the right panel.**

565 The multi-angular approach provides additional information for each pixel and constrains the forward model to match all the angular radiances at once. Indeed, the OSIRIS multi-angular characteristics have the advantage of decreasing the angular effects around the cloud bow directions by adding the contribution of other geometries. It avoids most of the failed convergences that occurred with the MODIS-like method and retrieved more homogeneous and coherent COT and $R_{eff}$ fields.

570 **6 Conclusions**

In this study, we present a method to retrieve retrieve two important microphysical and optical parameters of liquid clouds, COT and $R_{eff}$ and their uncertainties using NIR/SWIR multi-angular airborne measurements. The algorithm is based on the mathematical framework of the optimal estimation method (Rodgers, 2000) and focuses on assessing the different uncertainties on the retrieved properties originating from different sources of errors.

575 The studied case uses the measurements of the airborne radiometer OSIRIS obtained during the CALIOSIRIS campaign. It consists of a monolayer water cloud located at 5 km altitude over the ocean with tilted solar incidence ($\theta_s$=59°).

In the first step of the retrieval, COT and $R_{eff}$ are retrieved by considering only the measurement error (without introducing any error linked to the forward model).The uncertainties originating from different sources of error are

580 computed afterward by using the previously retreved COT and $R_{eff}$, and are decomposed into 3 different sources related to (a) the instrument measurement errors, (b) an incorrect estimation of the fixed model parameters such as the ocean surface wind, the cloud altitude and the effective variance of water droplets distribution, and (c) the errors related to the vertical and horizontal homogeneous cloud assumptions. The computations are done using the multi-angular

method and for comparison a mono-angular method, which is the usual approach in the operational algorithm called
585   here the MODIS-like algorithm.

In the multi-angular retrieval, a 5% measurement error contributes to around 3% of uncertainty on the retrieved COT and 6% on the retrieved $R_{eff}$. It increases with increasing values of COT and $R_{eff}$ for which the sensitivity of radiances starts to decrease. These uncertainties are doubled when considering a mono-angular retrieval. The uncertainties related to the fixed parameters remain low with both mono or multi-angular retrieval. The largest one
590   is due to the miss-knowledge of the effective variance of the droplet size and is respectively equal to 0.15% and 0.25% for the mono and multi angular case.

This study clearly shows that the largest uncertainty is due to the homogeneous cloud assumption made in our forward model. First, the uncertainties related to the homogeneous vertical profile were quantified using a heterogeneous LWC profile with a triangle shape (known as quasi-adiabatic) composed of two adiabatic profiles. This more realistic profile
595   takes into account the transition zone at the top of the cloud related to turbulent and evaporation processes. The scene averaged values reach 5% and 13% for COT and $R_{eff}$ respectively in the multi-angular retrieval of our case study and go up to 13% and 54% for COT and $R_{eff}$ respectively when using mono-angular measurements. The largest uncertainties are obtained for the largest cloud optical thickness as the radiations sample only the higher layers of the cloud where the information is different between the homogeneous and heterogeneous vertical profiles.

600   The other source of uncertainty related to the simplified cloud physical model comes from the radiatively non-independence of cloudy columns that dominate at the high spatial resolution of OSIRIS. In the optically thin overcast cloud case, studied here, the scene average uncertainties originating from the 3D effects are 4% for COT and 9% for $R_{eff}$ when using multi-angular measurements, and 28% for COT and 45% for $R_{eff}$ when using mono-angular measurements. The non-independence of the cloud columns dominates and tends to smooth the 3D radiative field
605   compared to radiances computed with the independent pixel approximation. Moreover, at the high solar incidence (59°), illumination and shadowing effects can be present. However, the use of multi-angular measurements mitigated their effects. Consequently, the uncertainties are lower when using multi-angular measurements.

The method presented here addressed the exploitation of OSIRIS and can be easily adapted to the future 3MI imager. The first step that consists of including the uncertainties related to the measurement errors is implementable in an
610   operational algorithm. The second step that consists of computing the uncertainties resulting from the cloud model is computationally expensive but can be applied to case studies to obtain a distribution of the error according to the cloud characteristic. In addition, the results obtained in this study show, not surprisingly regarding the numerous studies already published, that the vertical and horizontal homogeneity assumptions are major contributors to the retrieval uncertainties. One way to reduce it would be to define a more complex cloud model that can take into account the
615   vertical and horizontal heterogeneity. This adds more complexity in the forward model as it would implies to retrieve more sophisticated cloud parameters (e.g. extinction or effective size profile). It appears however possible given the important and complementary information provided by OSIRIS or 3MI measurements but more sophisticated retrieval methods need to be developed. Recent studies were proposed to retrieved vertical profile using cloud side information (Ewald et al., 2018; Alexandrov et al., 2020) or to realize multi-pixels retrieval to account for the non-independence of
620   the cloudy pixels (Martin et al., 2014; Okamura et al., 2017; Levis et al., 2015).

**Acknowledgements:** The authors thank Guillaume Merlin and Anthony Davis for fruitful discussions concerning the cloud vertical heterogeneous profile. This work has been supported by the Programme National de Télédétection Spatiale (PNTS, http://www.insu.cnrs.fr/pnts ), grant n° PNTS-2017-03 and by the CPER research project CLIMIBIO. The authors thank the French Ministère de l'Enseignement Supérieur et de la Recherche, the Hauts-de-France Region
625    and the European Funds for Regional Economical Development for their financialsupport to this project.

## References

Alexandrov, M. D., Cairns, B., Emde, C., Ackerman, A. S., and van Diedenhoven, B.: Accuracy assessments of cloud droplet size retrievals from polarized reflectance measurements by the research scanning polarimeter, 125, 92–111, https://doi.org/10.1016/j.rse.2012.07.012, 2012.

630    Alexandrov, M. D., Miller, D. J., Rajapakshe, C., Fridlind, A., van Diedenhoven, B., Cairns, B., Ackerman, A. S., and Zhang, Z.: Vertical profiles of droplet size distributions derived from cloud-side observations by the research scanning polarimeter: Tests on simulated data, 239, 104924, https://doi.org/10.1016/j.atmosres.2020.104924, 2020.

Auriol, F., Léon, J.-F., Balois, J.-Y., Verwaerde, C., François, P., Riedi, J., Parol, F., Waquet, F., Tanré, D., and Goloub, P.: Multidirectional visible and shortwave infrared polarimeter for atmospheric aerosol and cloud observation: OSIRIS (Observing
635    System Including PolaRisation in the Solar Infrared Spectrum), 71491D, https://doi.org/10.1117/12.806421, 2008.

Benner, T. C. and Evans, K. F.: Three-dimensional solar radiative transfer in small tropical cumulus fields derived from high-resolution imagery, 106, 14975–14984, https://doi.org/10.1029/2001JD900158, 2001.

Boucher, O., Randall, D., Artaxo, P., Bretherton, C., Feingold, G., Forster, P., Kerminen, V.-M., Kondo, Y., Liao, H., Lohmann, U., Rasch, P., Satheesh, S. K., Sherwood, S., Stevens, B., and Zhang, X. Y.: Clouds and Aerosols. In: Climate Change 2013: The
640    Physical Science Basis. Contribution of Working Group I to the Fifth Assessment Report of the Intergovernmental Panel on Climate Change [Stocker et al. (eds.)], Cambridge University Press, Cambridge, United Kingdom and New York, NY, USA, 571–658 pp., https://doi.org/10.1017/CBO9781107415324, 2013.

Bréon, F.-M. and Goloub, P.: Cloud droplet effective radius from spaceborne polarization measurements, 25, 1879–1882, https://doi.org/10.1029/98GL01221, 1998.

645    Buriez, J. C., Vanbauce, C., Parol, F., Goloub, P., Herman, M., Bonnel, B., Fouquart, Y., Couvert, P., and Seze, G.: Cloud detection and derivation of cloud properties from POLDER, 18, 2785–2813, https://doi.org/10.1080/014311697217332, 1997.

Cahalan, R. F., Ridgway, W., Wiscombe, W. J., Gollmer, S., and Harshvardhan: Independent Pixel and Monte Carlo Estimates of Stratocumulus Albedo, 51, 3776–3790, https://doi.org/10.1175/1520-0469(1994)051<3776:IPAMCE>2.0.CO;2, 1994.

Chang, F.: Estimating the vertical variation of cloud droplet effective radius using multispectral near-infrared satellite
650    measurements, 107, 4257, https://doi.org/10.1029/2001JD000766, 2002.

Chang, I. and Christopher, S. A.: Identifying Absorbing Aerosols above Clouds from the Spinning Enhanced Visible and Infrared Imager Coupled with NASA A-Train Multiple Sensors, 54, 3163–3173, https://doi.org/10.1109/TGRS.2015.2513015, 2016.

Cho, H., Zhang, Z., Meyer, K., Lebsock, M., Platnick, S., Ackerman, A. S., Di Girolamo, L., C.-Labonnote, L., Cornet, C., Riedi, J., and Holz, R. E.: Frequency and causes of failed MODIS cloud property retrievals for liquid phase clouds over global oceans,
655    120, 4132–4154, https://doi.org/10.1002/2015JD023161, 2015.

Cooper, S. J., L'Ecuyer, T. S., and Stephens, G. L.: The impact of explicit cloud boundary information on ice cloud microphysical property retrievals from infrared radiances, 108, n/a-n/a, https://doi.org/10.1029/2002JD002611, 2003.

Cornet, C. and Davies, R.: Use of MISR measurements to study the radiative transfer of an isolated convective cloud: Implications for cloud optical thickness retrieval, 113, 1–11, https://doi.org/10.1029/2007JD008921, 2008.

660 Cornet, C., Buriez, J., Riédi, J., Isaka, H., and Guillemet, B.: Case study of inhomogeneous cloud parameter retrieval from MODIS data, 32, L13807, https://doi.org/10.1029/2005GL022791, 2005.

Cornet, C., C-Labonnote, L., and Szczap, F.: Three-dimensional polarized Monte Carlo atmospheric radiative transfer model (3DMCPOL): 3D effects on polarized visible reflectances of a cirrus cloud, 111, 174–186, https://doi.org/10.1016/j.jqsrt.2009.06.013, 2010.

665 Cornet, C., C.-Labonnote, L., Waquet, F., Szczap, F., Deaconu, L., Parol, F., Vanbauce, C., Thieuleux, F., and Riédi, J.: Cloud heterogeneity on cloud and aerosol above cloud properties retrieved from simulated total and polarized reflectances, 11, 3627–3643, https://doi.org/10.5194/amt-11-3627-2018, 2018.

Cox, C. and Munk, W.: Measurement of the Roughness of the Sea Surface from Photographs of the Sun's Glitter, 44, 838, https://doi.org/10.1364/JOSA.44.000838, 1954.

670 Davis, A., Marshak, A., Cahalan, R., and Wiscombe, W.: The Landsat Scale Break in Stratocumulus as a Three-Dimensional Radiative Transfer Effect: Implications for Cloud Remote Sensing, 54, 241–260, https://doi.org/10.1175/1520-0469(1997)054<0241:TLSBIS>2.0.CO;2, 1997.

Deschamps, P.-Y., Breon, F.-M., Leroy, M., Podaire, A., Bricaud, A., Buriez, J.-C., and Seze, G.: The POLDER mission: instrument characteristics and scientific objectives, 32, 598–615, https://doi.org/10.1109/36.297978, 1994.

675 Elsaesser, G. S. and Kummerow, C. D.: Toward a Fully Parametric Retrieval of the Nonraining Parameters over the Global Oceans, 47, 1599–1618, https://doi.org/10.1175/2007JAMC1712.1, 2008.

Ewald, F., Zinner, T., Kölling, T., and Mayer, B.: Remote Sensing of Cloud Droplet Radius Profiles using solar reflectance from cloud sides. Part I: Retrieval development and characterization, 1–35, https://doi.org/10.5194/amt-2018-234, 2018.

Formenti, P., D'Anna, B., Flamant, C., Mallet, M., Piketh, S. J., Schepanski, K., Waquet, F., Auriol, F., Brogniez, G., Burnet, F.,
680 Chaboureau, J.-P., Chauvigné, A., Chazette, P., Denjean, C., Desboeufs, K., Doussin, J.-F., Elguindi, N., Feuerstein, S., Gaetani, M., Giorio, C., Klopper, D., Mallet, M. D., Nabat, P., Monod, A., Solmon, F., Namwoonde, A., Chikwililwa, C., Mushi, R., Welton, E. J., and Holben, B.: The Aerosols, Radiation and Clouds in Southern Africa Field Campaign in Namibia: Overview, Illustrative Observations, and Way Forward, 100, 1277–1298, https://doi.org/10.1175/BAMS-D-17-0278.1, 2019.

Garnier, A., Pelon, J., Dubuisson, P., Faivre, M., Chomette, O., Pascal, N., and Kratz, D. P.: Retrieval of Cloud Properties Using
685 CALIPSO Imaging Infrared Radiometer. Part I: Effective Emissivity and Optical Depth, 51, 1407–1425, https://doi.org/10.1175/JAMC-D-11-0220.1, 2012.

Giraud, V., Buriez, J. C., Fouquart, Y., Parol, F., and Seze, G.: Large-scale analysis of cirrus clouds from AVHRR data: Assessment of both a microphysical index and the cloud-top temperature, 36, 664–675, https://doi.org/10.1175/1520-0450-36.6.664, 1997.

De Haan, J., Bosma, P., and Hovenier, J.: The adding method for multiple scattering calculations of polarized light, 183, 371–391,
690 1987.

Hansen, J. E. and Travis, L. D.: Light scattering in planetary atmospheres, 16, 527–610, https://doi.org/10.1007/BF00168069, 1974.

Hickey, J. R. and Karoli, A. R.: Radiometric Calibrations for the Earth Radiation Budget Experiment, 13, 523, https://doi.org/10.1364/AO.13.000523, 1974.

695 Van de Hulst, H. C.: A new look at multiple scattering, Tech. Rep., Goddard Institute for Space Studies, NASA TM-I03044, 81 pp., 1963.

Inoue, T.: On the Temperature and Effective Emissivity Determination of Semi-Transparent Cirrus Clouds by Bi-Spectral Measurements in the 10&mu;m Window Region, 63, 88–99, https://doi.org/10.2151/jmsj1965.63.1_88, 1985.

Iwabuchi, H., Saito, M., Tokoro, Y., Putri, N. S., and Sekiguchi, M.: Retrieval of radiative and microphysical properties of clouds from multispectral infrared measurements, 3, 32, https://doi.org/10.1186/s40645-016-0108-3, 2016.

Kato, S. and Marshak, A.: Solar zenith and viewing geometry-dependent errors in satellite retrieved cloud optical thickness: Marine stratocumulus case, 114, 1–13, https://doi.org/10.1029/2008JD010579, 2009.

Kaufman, Y. J., Tanré, D., and Boucher, O.: A satellite view of aerosols in the climate system, 419, 215–223, https://doi.org/10.1038/nature01091, 2002.

Kokhanovsky, A. and Rozanov, V. V: Atmospheric Measurement Techniques Droplet vertical sizing in warm clouds using passive optical measurements from a satellite, 5, 517–528, https://doi.org/10.5194/amt-5-517-2012, 2012.

Levenberg, K.: A method for the solution of certain non-linear problems in least squares, 2, 164–168, https://doi.org/10.1090/qam/10666, 1944.

Levis, A., Schechner, Y. Y., Aides, A., and Davis, A. B.: An Efficient Approach for Optical Radiative Transfer Tomography using the Spherical Harmonics Discrete Ordinates Method, 1–17, 2015.

Lohmann, U. and Feichter, J.: Global indirect aerosol effects: a review, 5, 715–737, https://doi.org/10.5194/acp-5-715-2005, 2005.

Mallet, M., Dulac, F., Formenti, P., Nabat, P., Sciare, J., Roberts, G., Pelon, J., Ancellet, G., Tanré, D., Parol, F., Denjean, C., Brogniez, G., di Sarra, A., Alados-Arboledas, L., Arndt, J., Auriol, F., Blarel, L., Bourrianne, T., Chazette, P., Chevaillier, S., Claeys, M., D&apos;Anna, B., Derimian, Y., Desboeufs, K., Di Iorio, T., Doussin, J.-F., Durand, P., Féron, A., Freney, E., Gaimoz, C., Goloub, P., Gómez-Amo, J. L., Granados-Muñoz, M. J., Grand, N., Hamonou, E., Jankowiak, I., Jeannot, M., Léon, J.-F., Maillé, M., Mailler, S., Meloni, D., Menut, L., Momboisse, G., Nicolas, J., Podvin, T., Pont, V., Rea, G., Renard, J.-B., Roblou, L., Schepanski, K., Schwarzenboeck, A., Sellegri, K., Sicard, M., Solmon, F., Somot, S., Torres, B., Totems, J., Triquet, S., Verdier, N., Verwaerde, C., Waquet, F., Wenger, J., and Zapf, P.: Overview of the Chemistry-Aerosol Mediterranean Experiment/Aerosol Direct Radiative Forcing on the Mediterranean Climate (ChArMEx/ADRIMED) summer 2013 campaign, 16, 455–504, https://doi.org/10.5194/acp-16-455-2016, 2016.

Marquardt, D. W.: An Algorithm for Least-Squares Estimation of Nonlinear Parameters, 11, 431–441, https://doi.org/10.1137/0111030, 1963.

Marshak, A., Davis, A., Wiscombe, W., and Cahalan, R.: Radiative smoothing in fractal clouds, 100, 26247, https://doi.org/10.1029/95JD02895, 1995a.

Marshak, A., Davis, A., Wiscombe, W., and Titov, G.: The verisimilitude of the independent pixel approximation used in cloud remote sensing, 52, 71–78, https://doi.org/10.1016/0034-4257(95)00016-T, 1995b.

Marshak, A., Martins, J. V, Zubko, V., and Kaufman, Y. J.: Atmospheric Chemistry and Physics What does reflection from cloud sides tell us about vertical distribution of cloud droplet sizes?, Atmos. Chem. Phys, 5295–5305 pp., 2006a.

Marshak, A., Platnick, S., Várnai, T., Wen, G., and Cahalan, R. F.: Impact of three-dimensional radiative effects on satellite retrievals of cloud droplet sizes, 111, D09207, https://doi.org/10.1029/2005JD006686, 2006b.

Martin, W., Cairns, B., and Bal, G.: Adjoint methods for adjusting three-dimensional atmosphere and surface properties to fit multi-angle/multi-pixel polarimetric measurements, 144, 68–85, https://doi.org/10.1016/j.jqsrt.2014.03.030, 2014.

McClatchey, R. A., Fenn, R. W., Selby, J. E. A., Volz, F. E., and Garing, J. S.: Optical Properties of the Atmosphere (Third Edition), 1972.

Merlin, G.: Préparation à l'exploitation des observationsmulti-spectrales, multi-angulaires et polarisées de l'instrument 3MI pour les atmosphères nuageuses, University of Lille, 2016.

Miles, N. L., Verlinde, J., and Clothiaux, E. E.: Cloud Droplet Size Distributions in Low-Level Stratiform Clouds, 2000.

Miller, D. J., Zhang, Z., Ackerman, A. S., Platnick, S., and Baum, B. A.: The impact of cloud vertical profile on liquid water path retrieval based on the bispectral method: A theoretical study based on large-eddy simulations of shallow marine boundary layer clouds, 121, 4122–4141, https://doi.org/10.1002/2015JD024322, 2016.

Nakajima, T. and King, M. D.: Determination of the Optical Thickness and Effective Particle Radius of Clouds from Reflected Solar Radiation Measurements. Part I: Theory, 47, 1878–1893, https://doi.org/10.1175/1520-0469(1990)047<1878:DOTOTA>2.0.CO;2, 1990.

Nakajima, T. Y., Suzuki, K., and Stephens, G. L.: Droplet Growth in Warm Water Clouds Observed by the A-Train. Part II: A Multisensor View, 67, 1897–1907, https://doi.org/10.1175/2010JAS3276.1, 2010.

Okamura, R., Iwabuchi, H., and Sebastian Schmidt, K.: Feasibility study of multi-pixel retrieval of optical thickness and droplet effective radius of inhomogeneous clouds using deep learning, 10, 4747–4759, https://doi.org/10.5194/amt-10-4747-2017, 2017.

Oreopoulos, L. and Davies, R.: Plane Parallel Albedo Biases from Satellite Observations. Part I: Dependence on Resolution and Other Factors, 11, 919–932, https://doi.org/10.1175/1520-0442(1998)011<0919:PPABFS>2.0.CO;2, 1998.

Oreopoulos, L. and Platnick, S.: Radiative susceptibility of cloudy atmospheres to droplet number perturbations: 2. Global analysis from MODIS, 113, D14S21, https://doi.org/10.1029/2007JD009655, 2008.

Parol, F., Buriez, J. C., Brogniez, G., and Fouquart, Y.: Information Content of AVHRR Channels 4 and 5 with Respect to the Effective Radius of Cirrus Cloud Particles, 30, 973–984, https://doi.org/10.1175/1520-0450-30.7.973, 1991.

Platnick, S.: Vertical photon transport in cloud remote sensing problems, 105, 22919–22935, https://doi.org/10.1029/2000JD900333, 2000.

Platnick, S., King, M. D., Ackerman, S. A., Menzel, W. P., Baum, B. A., Riedi, J. C., and Frey, R. A.: The MODIS cloud products: algorithms and examples from terra, 41, 459–473, https://doi.org/10.1109/TGRS.2002.808301, 2003.

Poulsen, C. A., Siddans, R., Thomas, G. E., Sayer, A. M., Grainger, R. G., Campmany, E., Dean, S. M., Arnold, C., and Watts, P. D.: Cloud retrievals from satellite data using optimal estimation: evaluation and application to ATSR, 5, 1889–1910, https://doi.org/10.5194/amt-5-1889-2012, 2012.

Rivoire, L., Birner, T., Knaff, J. A., and Tourville, N.: Quantifying the Radiative Impact of Clouds on Tropopause Layer Cooling in Tropical Cyclones, 33, 6361–6376, https://doi.org/10.1175/JCLI-D-19-0813.1, 2020.

Rodgers, C. D.: Retrieval of atmospheric temperature and composition from remote measurements of thermal radiation, 14, 609, https://doi.org/10.1029/RG014i004p00609, 1976.

Rodgers, C. D.: Inverse methods for atmospheric sounding: Theory and Practice/Series on Atmospheric, Oceanic and Planetary Physics, in: Inverse Methods for Atmospheric Sounding, vol. 2, WORLD SCIENTIFIC, https://doi.org/10.1142/9789812813718_0001, 2000.

Seethala, C. and Horváth, Á.: Global assessment of AMSR-E and MODIS cloud liquid water path retrievals in warm oceanic clouds, 115, D13202, https://doi.org/10.1029/2009JD012662, 2010.

Sourdeval, O., -Labonnote, L. C., Brogniez, G., Jourdan, O., Pelon, J., and Garnier, A.: A variational approach for retrieving ice cloud properties from infrared measurements: application in the context of two IIR validation campaigns, 13, 8229–8244, https://doi.org/10.5194/acp-13-8229-2013, 2013.

Sourdeval, O., C.-Labonnote, L., Baran, A. J., and Brogniez, G.: A methodology for simultaneous retrieval of ice and liquid water cloud properties. Part I: Information content and case study, 141, 870–882, https://doi.org/10.1002/qj.2405, 2015.

Szczap, F., Isaka, H., Saute, M., Guillemet, B., and Ioltukhovski, A.: Effective radiative properties of bounded cascade absorbing clouds: Definition of an effective single-scattering albedo, 105, 20635–20648, https://doi.org/10.1029/2000JD900145, 2000.

Takahashi, H., Lebsock, M., Suzuki, K., Stephens, G., and Wang, M.: An investigation of microphysics and subgrid-scale variability in warm-rain clouds using the A-Train observations and a multiscale modeling framework, 122, 7493–7504, https://doi.org/10.1002/2016JD026404, 2017.

780    Twomey, S.: Aerosols, clouds and radiation, 25, 2435–2442, https://doi.org/10.1016/0960-1686(91)90159-5, 1991.

Várnai, T.: Influence of three-dimensional radiative effects on the spatial distribution of shortwave cloud reflection, 57, 216–229, https://doi.org/10.1175/1520-0469(2000)057<0216:IOTDRE>2.0.CO;2, 2000.

Várnai, T. and Davies, R.: Effects of Cloud Heterogeneities on Shortwave Radiation: Comparison of Cloud-Top Variability and Internal Heterogeneity, 56, 4206–4224, https://doi.org/10.1175/1520-0469(1999)056<4206:EOCHOS>2.0.CO;2, 1999.

785    Várnai, T. and Marshak, A.: Observations of Three-Dimensional Radiative Effects that Influence MODIS Cloud Optical Thickness Retrievals, 59, 1607–1618, https://doi.org/10.1175/1520-0469(2002)059<1607:OOTDRE>2.0.CO;2, 2002.

Várnai, T. and Marshak, A.: A method for analyzing how various parts of clouds influence each other's brightness, 108, 4706, https://doi.org/10.1029/2003JD003561, 2003.

Várnai, T. and Marshak, A.: View angle dependence of cloud optical thicknesses retrieved by Moderate Resolution Imaging
790    Spectroradiometer (MODIS), 112, 1–12, https://doi.org/10.1029/2005JD006912, 2007.

Várnai, T. and Marshak, A.: MODIS observations of enhanced clear sky reflectance near clouds, 36, L06807, https://doi.org/10.1029/2008GL037089, 2009.

Wang, C., Platnick, S., Zhang, Z., Meyer, K., and Yang, P.: Retrieval of ice cloud properties using an optimal estimation algorithm and MODIS infrared observations: 1. Forward model, error analysis, and information content, 121, 5809–5826,
795    https://doi.org/10.1002/2015JD024526, 2016.

Wood, R.: Drizzle in Stratiform Boundary Layer Clouds. Part II: Microphysical Aspects, 62, 3034–3050, https://doi.org/10.1175/JAS3530.1, 2005.

Yang, Q., Fu, Q., and Hu, Y.: Radiative impacts of clouds in the tropical tropopause layer, 115, 1–21, https://doi.org/10.1029/2009JD012393, 2010.

800    Zhang, Y., Xie, S., Lin, W., Klein, S. A., Zelinka, M., Ma, P., Rasch, P. J., Qian, Y., Tang, Q., and Ma, H.: Evaluation of Clouds in Version 1 of the E3SM Atmosphere Model With Satellite Simulators, 11, 1253–1268, https://doi.org/10.1029/2018MS001562, 2019.

Zhang, Z. and Platnick, S.: An assessment of differences between cloud effective particle radius retrievals for marine water clouds from three MODIS spectral bands, 116, D20215, https://doi.org/10.1029/2011JD016216, 2011.

805    Zhang, Z., Ackerman, A. S., Feingold, G., Platnick, S., Pincus, R., and Xue, H.: Effects of cloud horizontal inhomogeneity and drizzle on remote sensing of cloud droplet effective radius: Case studies based on large-eddy simulations, 117, n/a-n/a, https://doi.org/10.1029/2012JD017655, 2012.

Zinner, T. and Mayer, B.: Remote sensing of stratocumulus clouds: Uncertainties and biases due to inhomogeneity, 111, D14209, https://doi.org/10.1029/2005JD006955, 2006.

810